

Infrared Colors of Trans-Neptunian Objects Observed with HST

Joseph Rawlins

A senior thesis submitted to the faculty of
Brigham Young University
in partial fulfillment of the requirements for the degree of
Bachelor of Science

Dr. Denise Stephens, Advisor

Department of Physics and Astronomy

Brigham Young University

August 2011

Copyright © 2011 Joseph Rawlins

All Rights Reserved

ABSTRACT

Infrared Colors of Trans-Neptunian Objects Observed with HST

Joseph Rawlins
Department of Physics and Astronomy
Bachelor of Science

We have analyzed 80 trans-Neptunian objects (TNOs) observed with the near-infrared camera and multi-object spectrometer (NICMOS) aboard the Hubble Space Telescope (HST) and measured their ($J - H$) near-IR (NIR) magnitudes and colors. We used a model psf fitting process to obtain our results. While the ($B - R$) color of TNOs show a clear difference in color for objects with inclination angles $< 6^\circ$ and those $> 6^\circ$, we find no such trends in the NIR ($J - H$) colors. Two of our objects are blue in the near-IR and have been identified with the Haumea collisional family. There are also hints of variability in (19255) 1999 VK₈, 1999 OE₄, 2000 CE₁₀₅, 1998 KG₆₂ and 1998 WX₃₁.

Keywords: Kuiper Belt, Color, trans-Neptunian, Infrared HST Observations

ACKNOWLEDGMENTS

I would like to thank Dr. Stephens for the opportunity to work on this project. She took me on to the project at a time when, academically speaking, I did not know what the Kuiper belt was. She has patiently explained various aspects of this project over and over and over and over and over again.

Ryan Porritt is a good friend who patiently explained the inner workings of IRAF and how to work from the command line. With the experience he had, he was able to help me understand what each program was doing and, in the process, instructed me in basic programming literacy. He was a valuable resource when Dr. Stephens was not available.

I want to thank BYU's astronomy department for access to all of their resources and wonderful faculty who have been patiently available to answer questions. The physics department office staff have been wonderfully and willingly helpful. They are a valuable resource to the college.

I express the most heartfelt gratitude for my wife and children who have patiently, ever so patiently, been with me through the last four years as I have pursued my education. My wife has endured many long days and nights by herself and yet she has been unwaveringly supportive. She has been an invaluable strength during times of difficulty and has lovingly helped the children understand what their dad was doing. She has brought them to campus so they could see what I was doing and so I could be with them for a short time. Without her confidence and faith, and the sweet prayers of my children, I would never have gotten to this point.

Ultimately, I express my most humble gratitude to the Lord for His tender mercies during my time here at school. He has always been willing to bless and assist, even when I have been very expressive of my frustrations. I have witnessed miracles. The completion of this thesis being one of them. His giving hand has supported and sustained me and my family in every aspect of our lives according to the promises He extended upon my return to school. I dedicate my education and my life to expressions of gratitude and love for God and His Beloved Son, Jesus Christ.

Contents

Table of Contents	iv
List of Figures	vi
1 Introduction - The Kuiper Belt	1
1.1 Discovery	1
1.2 Formation	2
1.2.1 Cold Population	4
1.2.2 Hot Population	4
1.3 Characteristics of Kuiper Belt Objects (KBOs)	6
1.3.1 Size	6
1.3.2 Chemical Composition	7
1.3.3 Light Source (Albedo)	8
1.3.4 Color	9
1.3.5 Orbital Dynamics	10
1.4 Motivation	12
2 Observations	13
2.1 Why Observe in Near-IR?	13
2.2 Equipment	14
2.2.1 Hubble Space Telescope (HST)	14
2.2.2 Near Infrared Camera and Multi-Object Spectrometer (NICMOS)	14
2.2.3 Data Reduction Pipeline	17
2.3 Observational Technique	18
3 Reduction Process	22
3.1 Photometry	22
3.1.1 Point Spread Modeling	23
3.1.2 Aperture Photometry	24
3.2 Data Reduction Process	25
4 Results and Conclusions	31

A TinyTim	37
B IRAF Parameters	41
Bibliography	44
Index	46

List of Figures

1.1	Position of the Kuiper Belt	2
1.2	Inclination vs. Distance	3
1.3	Kuiper belt formation models	4
1.4	Freezing points of various ices in the solar nebula	6
1.5	Frostline	7
1.6	Kuiper Belt and Orbital Resonance	12
2.1	Ice spectra	15
2.2	Atmospheric absorption of electromagnetic spectrum	16
2.3	Space vs. ground <i>J</i> and <i>H</i> bandwidths	17
2.4	Normalizing NICMOS camera frames with pedsky	19
2.5	Effectiveness of <i>JHHJ</i> observing pattern	20
2.6	Effectiveness of dithering	21
3.1	inpar.txt	28
3.2	Reduction Outline	30
4.1	Plot: Distance vs. Eccentricity	36
B.1	IRAF Parameters - Data	42

B.2 IRAF Parameters - Model 43

Chapter 1

Introduction - The Kuiper Belt

This chapter begins with a brief history of the discovery of the Kuiper belt and its relation to the rest of the solar system. I briefly discuss formation models that are used to explain the construct of the belt. I then detail various characteristics of Kuiper belt objects (KBO) and conclude with the motivation behind our project.

1.1 Discovery

The Kuiper belt is a collection of icy bodies that are remnants of the early formative stages of the solar system. It is a ring that lies beyond the eight traditional planets and extends from Neptune's orbit at 30 astronomical units (A.U.) to a distance of approximately 55 A.U. (see Figure 1.1).

In 1943 Kenneth Edgeworth first postulated the idea of a large reservoir of such objects beyond the planets. This idea arose from the observations of short-period comets, like Halley's comet, that were orbiting close to the plane of the solar system. Their association with the plane of the solar system led to Gerard Kuiper's prediction of the Kuiper belt in 1951. However, these objects are extremely faint because of their small sizes and great distances and could not be directly observed. It was not until 1992 that there was sufficiently sophisticated equipment to allow David Jewitt and

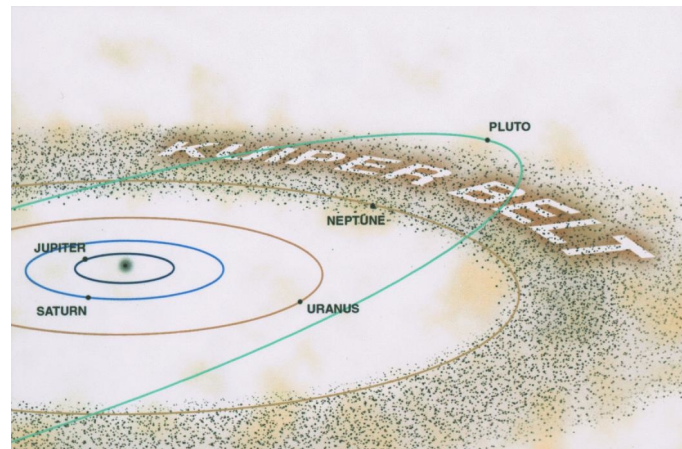


Figure 1.1 The Kuiper belt relative to the planets. Shown is Pluto's highly elliptical / inclined orbit. Image courtesy of: www.kiwispaceplace.com

Jane Luu at the University of Hawaii to observe the first one (Jewitt et al. 1992).

The Kuiper belt is subdivided into several categories by orbital parameters according to Gladman et al. (2008). The main focus of our research was in the classical belt, although objects from each category are included in the data set (see Table 4.1). The classical belt, itself, is divided into two subcategories - cold and hot. The cold classical belt is composed of objects with an orbital inclination (an angle measured with respect to the plane of the solar system) $< 6^\circ$ while objects with an inclination $> 6^\circ$ are grouped into the hot category (see Figure 1.2). The two populations seem to have slightly different ($B - R$) colors, which could suggest that they have different origins (see Section 1.2). Observational results such as this could help refine the current formation models of the solar system.

1.2 Formation

Current solar system formation models hold that a portion of a giant interstellar gas cloud condensed and began to spin, flattening into a disk, with a developing proto-star at the center. Within

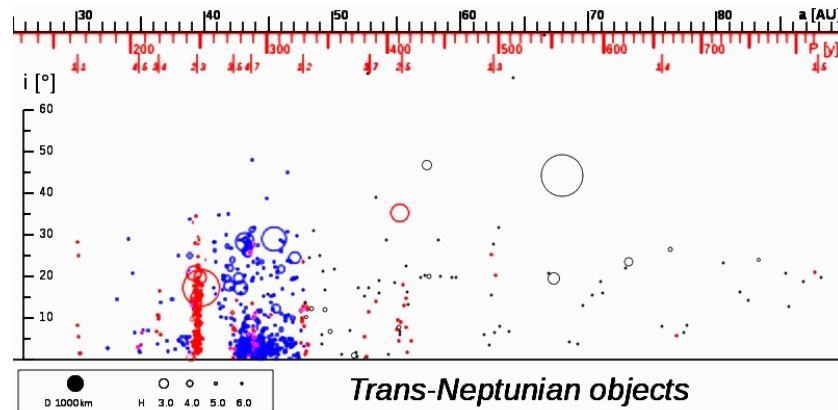


Figure 1.2 Inclination angle (i) vs. semi-major axis (A.U.). Several Gladman classifications can be seen: red = Resonant, blue = Classical, gray = Scattered Disk Objects (SDO). Image courtesy of: http://en.wikipedia.org/wiki/Kuiper_belt

this solar disk, particles began to coalesce and increase in size. Assuming an anisotropic distribution of gas and dust, particles in regions with higher density grew at a higher rate than those with lower density and developed into planets. Those whose rate of growth was not as great were scattered throughout the disk as asteroids and future KBOs. Lighter materials such as leftover gas and dust were blown out of the solar system by solar radiation.

The asteroids and KBOs were originally located throughout the early proto-planetary disk. However, interactions with the larger planets, as illustrated in Figure 1.3, scattered these objects, throwing some out of the solar system all together, some into the Oort cloud, and some on top of the original population of the Kuiper Belt. This behavior could produce two populations of objects: a dynamically "cold" population that originally formed beyond Neptune and a dynamically "hot" population that was scattered into the Kuiper Belt region. There are other populations that became trapped in resonant orbits with Neptune. These resonant objects, the cold and hot classical populations, and the objects scattered beyond the Kuiper Belt, called scattered disk objects (SDOs), make up the body of objects beyond Neptune (Morbidelli & Levison 2003). I will address only the cold and hot populations of the classical belt.

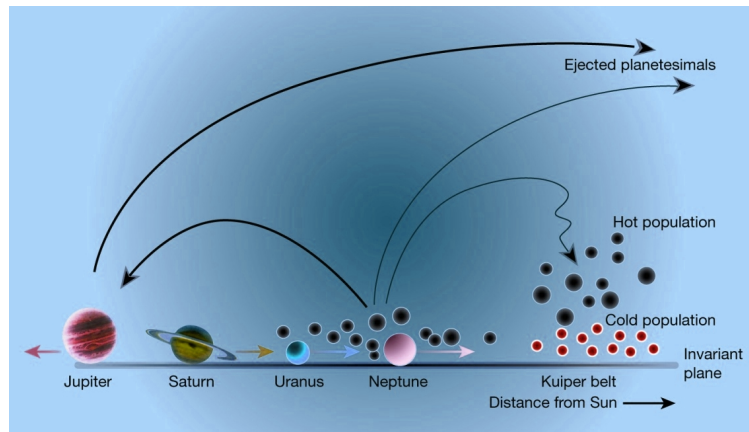


Figure 1.3 Migration and slingshot models of Kuiper belt formation. Shown are the hot and cold populations relative to solar plane. Image: Nature magazine (Morbidelli & Levison 2003)

1.2.1 Cold Population

As the solar system was forming, the planets and other smaller bodies - including the KBOs in the cold classical belt - orbited the proto-sun within the solar disk in compliance with Newton's laws of motion. Due to the preponderance of material in the proto-planetary disk, the developing planets were subject to collisions in the early, active stages of the solar system. These interactions caused the planets to move about in the solar disk. Throughout this process, the planets nudged smaller objects, like KBOs, into their current locations by gravitational interaction. Because of the gentle nature of these interactions, the positions of the planets relative to cold classical KBOs remained unchanged over time. Since this process occurred within the disk, this model is used to explain the low inclination angle of the cold classical belt seen in Figure 1.3 (Morbidelli & Levison 2003).

1.2.2 Hot Population

During the formation of the solar system objects that passed too close to a giant planet were scattered throughout the solar disk. Neptune directly interacted with the objects in its path via gravitational

Table 1.1. Freezing Points of Various Ices

Molecule	° C	K
H ₂ O	0	273.15
NH ₃	-77	196
CH ₄	-182.5	91

influence. Some of the smaller bodies were captured and joined Neptune's native moons. The remainder approached Neptune with velocities sufficiently fast that they were able to escape orbital capture. They entered Neptune's vicinity and were gravitationally assisted back out. Some were ejected completely from the solar system while others were tossed into other locations such as the hot classical belt shown in Figure 1.3. This model offers an explanation for why hot classical KBOs are found at higher inclinations (Morbidelli & Levison 2003).

These models suggest that the Kuiper belt is made up of objects that formed in different locations throughout the proto-planetary disk. If each of these populations has a different spatial origin, then a knowledge of their chemical composition can help us understand how the Kuiper belt and, therefore, the solar system formed. Observations of larger KBOs indicate that they are composed of water (H₂O), methane (CH₄), and ammonia (NH₃) ices (Tegler et al. 2007). Each of these ices has a different freezing point according to Table 1.1 and freezes at a different location in the solar system (see Figure 1.4 & 1.5).

Near the forming sun, the temperatures are too hot to form ice. However, at a point called the frost line, the temperatures are sufficiently cold that at approximately the location of Jupiter, water begins to condense. At Neptune's distance, methane ice begins to form and ammonia falls between these two. These different freezing points imply that objects that are predominantly composed of water ice formed farther in, those that have a dominant methane presence formed farther out, and

those with ammonia ices formed somewhere in between. Therefore, a knowledge of their chemical composition yields a great deal of information about the structure of the early solar system, the conditions that may have existed, and the migration of the giant planets responsible for scattering objects close to the sun out to greater distances.

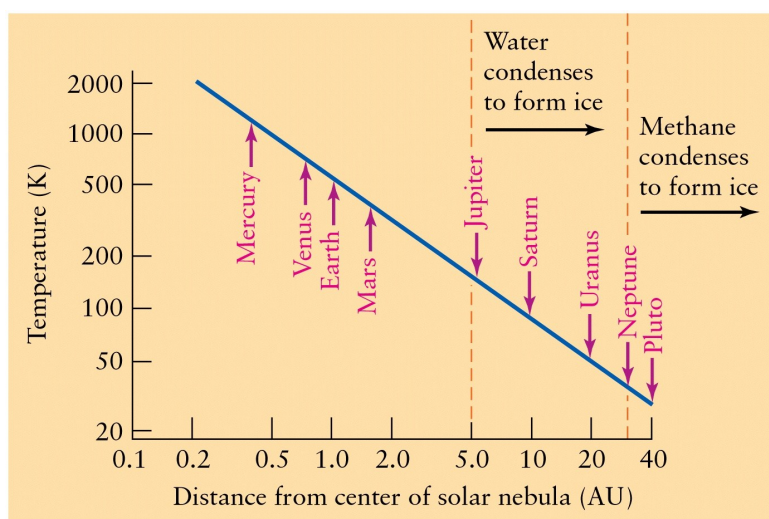


Figure 1.4 Freezing points of various ices in the solar nebula. Freezing points on Celsius and Kelvin scales can be found in Table 1.1. Image courtesy of Universe, 8th ed., 2008, Clancy Marshall.

1.3 Characteristics of Kuiper Belt Objects (KBOs)

1.3.1 Size

The sizes of KBOs vary greatly. The smallest detected to date is ~ 0.98 km (discovered by HST in December of 2009 by Schlichting et al. 2009), though it is anticipated that there are a great many more much smaller than this. Larger KBOs can reach sizes over 2000 km such as Pluto and Eris with diameters of 2322 km and 2340 km, respectively. Our data set includes objects that are in

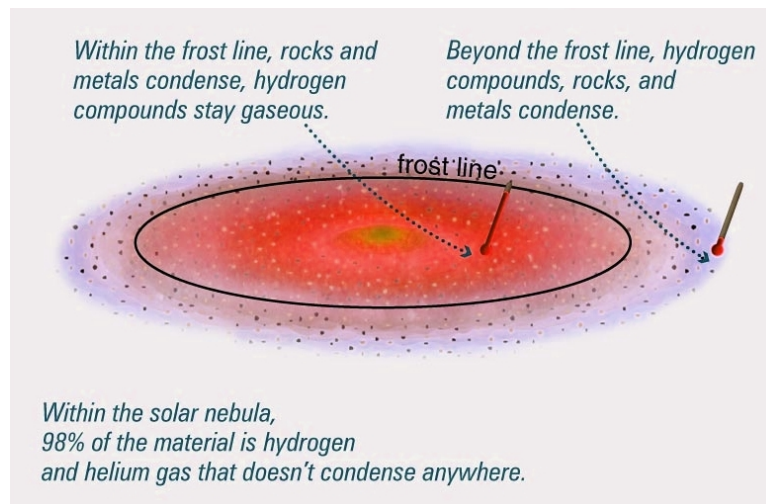


Figure 1.5 Approximate location of frostline lies between Mars and Jupiter. Image courtesy of Pearson Education Inc., 2005, Addison Wesley.

the range of about 100 km. Their size, and the sparse distribution of objects in the Kuiper belt, make them very difficult to detect. Preliminary detection from ground-based telescopes allowed for follow-up observations using the space-based Hubble Space Telescope (HST). But, even with HST, spectra cannot be taken because of their size, so we use photometric colors to infer chemical composition.

1.3.2 Chemical Composition

The chemical composition of the Kuiper belt is of great interest because of the understanding it can provide on how the solar system formed. While we were not working with spectra, spectral analysis has been performed on larger KBOs which has revealed much information about their composition (Tegler et al. 2007). From this previous work we can infer composition of smaller KBOs using photometric colors (Doressoundiram et al. 2008). Some of the elements that have been discovered to exist in the Kuiper belt are methane (CH_4), ammonia (NH_3) and water (H_2O) - all in ice form (See Section 1.2 for a discussion of these ices in the context of the formation of the

solar system).

However, because the Kuiper belt has remained relatively unchanged since the early stages of the solar system, and collisions are exceptionally rare, the vast majority of KBOs are covered with a hydrocarbon material. Early in the development of the solar system there was a lot of activity from the sun which sent out a bombardment of high-energy particles and photons. As these particles interacted with the surface ices of KBOs, they had the effect of knocking hydrogen atoms free through photodissociation. This created free molecular bonds which recombined into complex organic materials. As a result of this process, excess hydrocarbons built up with time and created a very dark surface, which is what we find now. Although this build-up interferes with detection of the ices themselves, knowing how the original ices decay through photodissociation can help determine what may lie at the core of a KBO (Hudson et al. 2008).

1.3.3 Light Source (Albedo)

According to Jewitt and Luu (2004), the temperature of the Kuiper belt is extremely cold with temperatures at or near 50 K so that the thermal radiation of KBOs peaks out at $\sim 60\mu\text{m}$. Attempting to observe Kuiper belt objects from the ground at these wavelengths is very difficult because the atmosphere is opaque to the near-infrared spectral features that occur in this range (Chapter 2 addresses this subject in more detail and I leave the nitty-gritty of this discussion for that section). The light we observe in the visible is not from the KBOs themselves. Rather, we observe sunlight reflected from their surfaces. However, the surface of a KBO is not a perfect reflector, so we do not receive a perfect reflection of the sun's spectrum. Fortunately, there are many absorption features superimposed on the reflected spectrum that are diagnostic of surface composition (see Figure 2.1). Therefore, the colors used to describe Kuiper belt objects are defined by how the sun's light interacts with the surface material of the KBOs.

1.3.4 Color

Because light we observe from KBOs is reflected sun light, color in the Kuiper belt is defined relative to the colors of the sun. So, when speaking of red or blue, it does not mean that the KBO is red or blue; it means that it is redder or bluer than some solar reference point. Additionally, because the light is reflected off the surface of a KBO, the implication is that color is composition dependent. In the Kuiper belt the vast majority of KBOs are red. So, what is meant when discussing red or blue in the Kuiper belt?

Red

The "red" indicates that something that is highly reflective at red wavelengths is covering the ice. This "something" is the hydrocarbons describe in Section 1.3.2 which arises from the process of photodissociation. The build-up of hydrocarbons on the surface results in a reflected spectrum very different from the sun (see Section 2.1). This build-up process occurred billions of years ago when the sun was very active. The red color suggests that there has been little modification to their surface. Therefore, KBOs have more or less remained in their current state since that time. Since hydrocarbons reflect more at longer wavelengths, to say that they are red simply means that we receive a greater percentage of reflected light at the red end of the spectrum. The material on a red KBO is actually much darker.

Blue

Blue indicates the presence of fresh ice on the surface. In such a case, some mechanism has removed hydrocarbons from the surface and exposed the ice beneath. The ices absorb more at longer wavelengths and reflect and scatter at the shorter. Similar to red, these objects are blue merely because they are brighter at shorter wavelengths. Approximately 3% of our data set is blue. This is likely due to collisions which break away the darker surface material, revealing fresh

sub-surface ice. A family of objects that fall into this category is named the Haumea collisional family (EL 61). In this case, the collision that created this blue family occurred four billion years ago (Ragozzine & Brown 2007), confirming the stable nature of the Kuiper belt.

Except in exceptionally rare cases like Haumea, blue simply means less red. Hydrocarbons are inclined to absorb bluer wavelengths while reflecting the redder wavelengths. So, when we observe them, what we see has been reddened. Even though the greater majority of KBOs are red by these definitions, some appear to be less red than others and these are what we call blue in this thesis.

As an example, Table 1.2 provides a sample of Table 4.1 wherein can be found the tabulated fullness of the results of the project. The $J - H$ colors of four objects are shown relative to that of the sun. Values that are greater than the sun's (0.42) are usually called red and values smaller than the sun's are usually called blue. Except in the case of the Haumea fragments, it can be seen that even the objects we're calling "blue" in this thesis have a higher index than the sun, indicating a red color. The "red" objects *also* have a higher value than the sun. Clearly, both groups are red. However, objects whose value are lower *relative* to their higher-valued counterparts are considered blue. One of the reasons for this is that it helps to identify any color variations that may occur in the Kuiper belt.

1.3.5 Orbital Dynamics

There is a great variety of orbital dynamics in the Kuiper belt and Gladman et al. (2008) describes these in detail. I provide a brief description of only those classifications that appear in our data set (see Table 4.1).

Cubewanos, more commonly known as classical objects, are classified as those objects whose distances range from 40 - 50 A.U. and whose orbits do not cross Neptune's. They have low-inclination orbits and low-eccentricity. Most of these objects are found in between the 2:3 and

Table 1.2. Sub-sample of Table 4.1

Object	$J - H$	Color
Sun	0.42	-
1999 OY ₃	-0.27	Haumea
1995 SM ₅₅	-0.16	Haumea
2000 CM ₁₀₅	0.49	Blue
1999 CH ₁₀₉	0.42	Blue
1994 VK ₈	0.73	Red
1997 CR ₂₉	0.70	Red

1:2 resonances of the Kuiper belt (see Figure 1.6). The resonant objects are simply those that have been captured in integer relation orbits with Neptune. Scattered disk objects (SDO) are those whose distances range from 30 A.U. out to as far as 100 A.U. This region overlaps the classical region and so several of these objects are included in our set. However, their inclinations can reach as high as 40 degrees. It is believed that they arrived at their current location because of scattering by the larger planets and are still subject to perturbations from Neptune. These perturbations can sometimes capture these objects in resonant orbits as well. Because of the relatively unstable nature of this region, it is believed that most periodic comets originate here (Morbidelli 2005). Finally, the plutinos are those objects that are in a 2:3 resonance with Neptune. They received the name plutino because Pluto falls in this group, with 2 Plutonian orbits to every 3 Neptunian.

This variety of classifications in our data set results in a large spread in inclination angles, ranging from tightly confined to the planetary plane to angles as large as 40 degrees. The highest angle in our data set was 31.7 degrees (object 96 RQ₂₀).

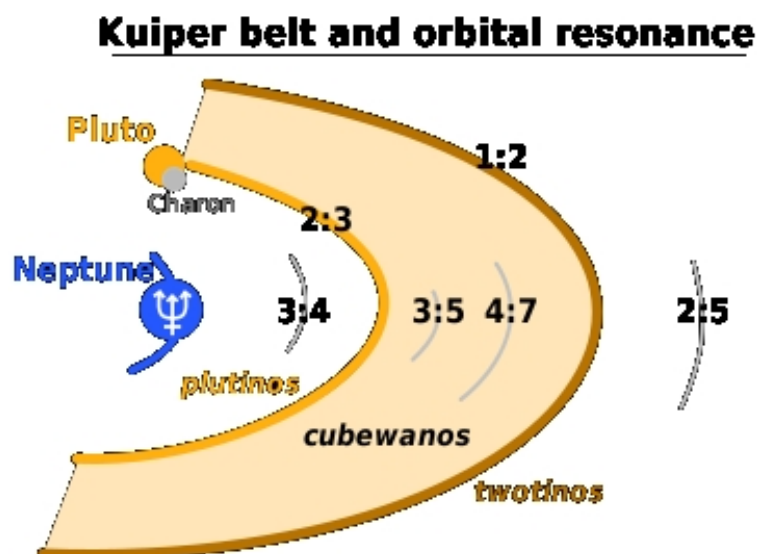


Figure 1.6 Various classifications and their orbital ratios relative to Neptune. Both plutinos and cubewanos are included in our data set. SDOs also fall in this region but have been omitted for clarity along with other classifications characterized by higher eccentricities. See also Figure 1.2. Image courtesy of: http://en.wikipedia.org/wiki/Kuiper_belt

1.4 Motivation

The Kuiper belt is a key to understanding the formation of the solar system. While much work has been done to identify the nature of KBOs, their size and distance impose limitations on spectral data collection. However, the photometric colors we obtained during our research are connected to their chemical and orbital properties as described. Increasing the data available allows us to refine the evolutionary models of the solar system and, therefore, the Kuiper belt as discussed in Section 1.2. Our data set augments previously published information with the largest space-based, near-infrared observations to date.

Chapter 2

Observations

In this chapter I will discuss the observational technique we used for our project, why we observed in the near-infrared (NIR) and why HST was selected as the instrument of choice. I mention some of the equipment HST used during observations, including cameras and filters, and conclude with a description of the technique used to optimize our observation time.

2.1 Why Observe in Near-IR?

Light we receive from KBOs in the optical and NIR is reflected sunlight. The surfaces of KBOs consist of the photodissociated ices of CH_4 , NH_3 , and H_2O (Jewitt & Luu 2004; Tegler et al. 2007). A signature portion of the incident light is preferentially absorbed by each of these molecules at different wavelengths in the near-infrared (see Figure 2.1). The absorption associated with an increase in energy in the ice molecules yields the spectral features of interest in the NIR. While we were not involved in obtaining spectra for these objects because of their size, our work did involve finding their photometric colors. Color is composition dependent. Therefore, *inferences* can be made about their chemical make-up and future follow-up spectral observations with larger telescopes (James Webb Space Telescope and the Thirty Meter Telescope) can verify the correlation

between color and ice. We observed in the NIR with the hope of detecting differences in their colors due to the various ices.

2.2 Equipment

2.2.1 Hubble Space Telescope (HST)

Hubble Space Telescope was selected as the instrument of choice for various reasons. One of the principle reasons was its advantage of being a space telescope. Our KBOs are very small and extremely dim. To observe them requires the ability to acquire all available light. Any obstruction, such as the earth's atmosphere, can frustrate this end. The wavelength range over which we were observing is especially susceptible because of water band absorption in the atmosphere (see Figure 2.2). Even for a large, earth-bound, telescope like Keck (10 m diameter primary mirror), which can gather a lot more light, it cannot replace light that has been absorbed by the atmosphere.

Additionally, HST had the NIR observing capabilities necessary for this project as discussed in the next section. The camera used by HST was the Near Infrared Camera and Multi Object Spectrometer (NICMOS) with a broad-band IR filter range of 0.8-2.45 μm .

2.2.2 Near Infrared Camera and Multi-Object Spectrometer (NICMOS)

NICMOS operates three NIR detectors, NIC1, NIC2 and NIC3, each with a different spatial resolution that reads out four independent quadrants each 128×128 pixels which combine to produce one 256×256 pixel array for each detector (Viana et al. 2009).

NIC1 has the best spatial resolution with an $11'' \times 11''$ field and 0.043'' pixels. NIC1 covers the NIR wavelength range of 0.8 to 1.8 μm which does not quite reach as far as was needed for our purposes.

NIC2 covers $19.2'' \times 19.2''$ of sky, with each pixel having a resolution of 0.075'' (Viana et al.

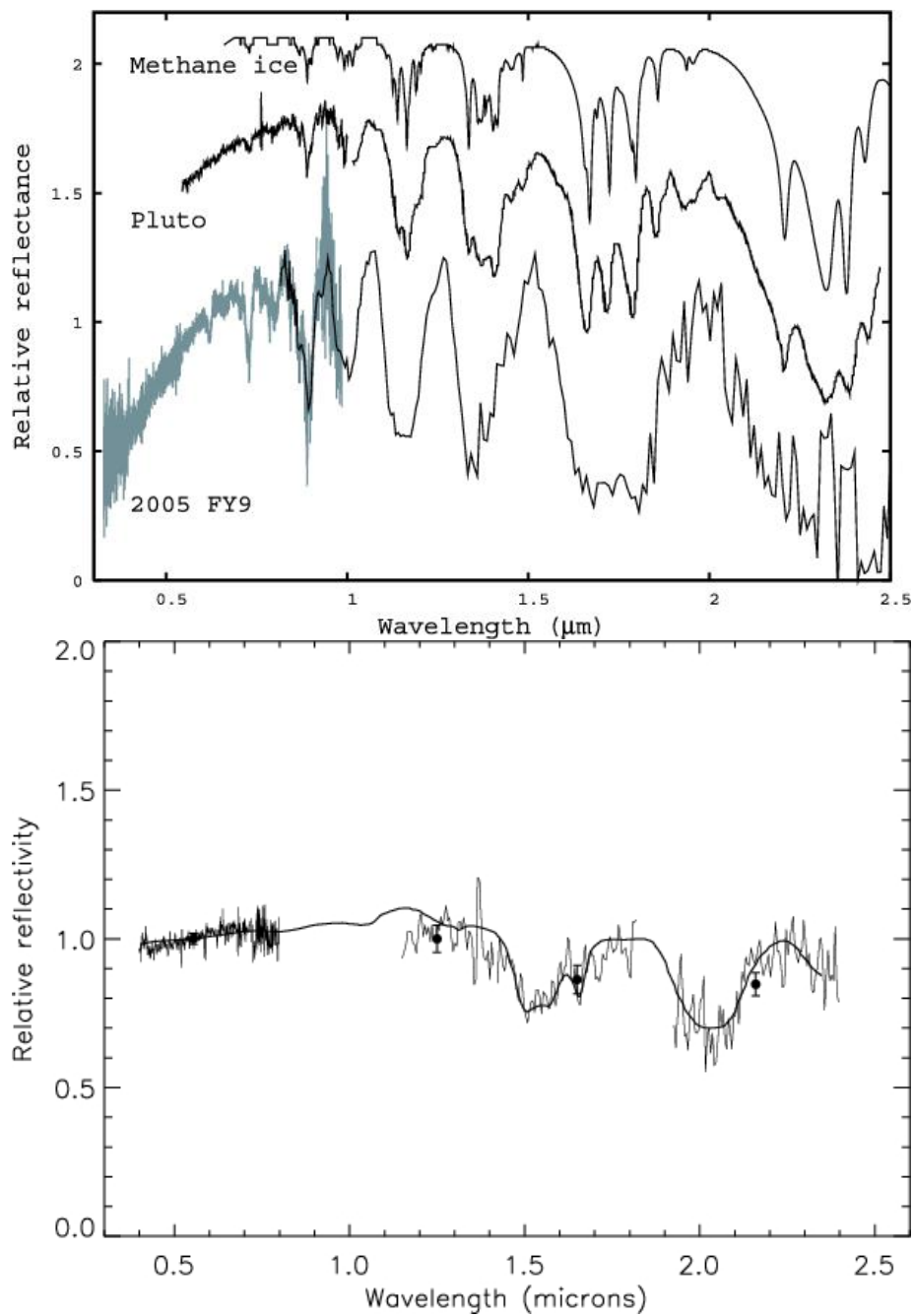


Figure 2.1 (Top) Methane ice absorption compared to other objects in the Kuiper belt: Pluto and 2005 FY9. Note major features at approx. 1.2, 1.3, 1.75, and 2.3 μm (Licandro et al. 2006). (Bottom) Water ice absorption compared to Orcus. Note major features at approx. 1.5 and 2.0 μm (de Bergh et al. 2005).

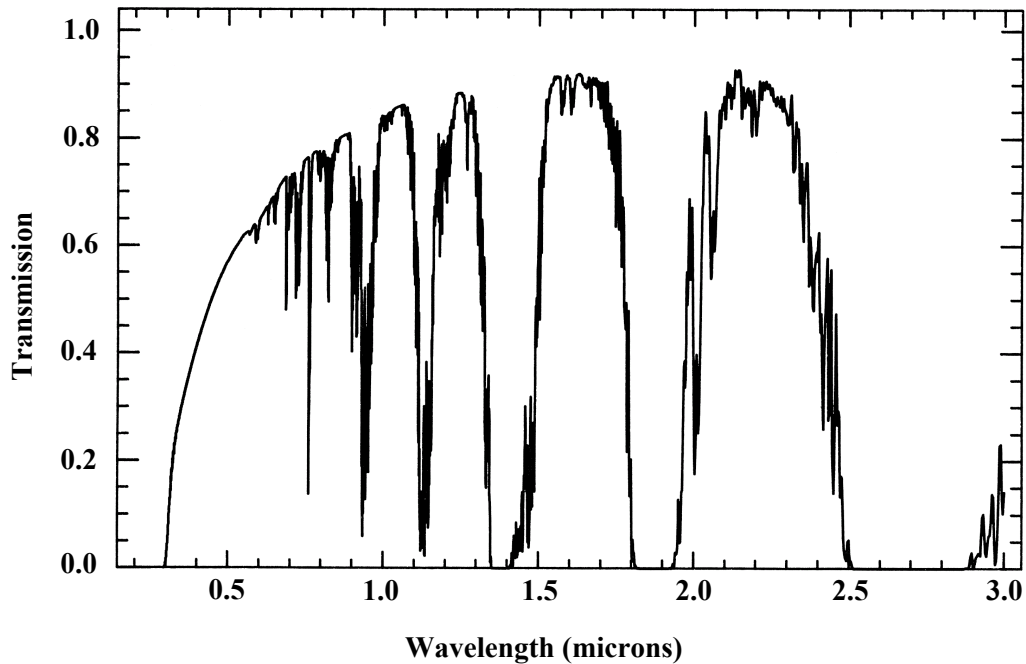


Figure 2.2 Atmospheric absorption due to H₂O and CO₂ molecules. Note the bands at 1.2, 1.3, and 1.75 μm where absorption features of interest occur (see Fig. 2.1). Image courtesy of [USGS](#) (Berk et al. 1989)

2009) and covers the broad spectral range of 0.8-2.45 μm . Compare this to the large 10 m Keck telescopes in Hawaii which also operate a NIR camera (NIRC) that images on a 256×256 array with 0.15"/pixel resolution (See Keck Telescope and Facility Instrument Guide, 2002, pg. 15). However, Keck's resolution is determined by the quality of atmospheric seeing. Although some NIR wavelengths do reach the ground, Figure 2.2 illustrates that Keck and other ground-based telescopes are restricted to narrow *J* and *H* filters that can "see" between those bands.

On the other hand, the NIC2 filters are not limited in size by the atmospheric H₂O bands because of HST's location *above* the atmosphere. The broad range *J* (F110W) and *H* (F160W) filters aboard NIC2 (see Figure 2.3) allow observers to maximize on the light output, which was needed for such dim objects. We selected these filters because they allow us to "see" the ice

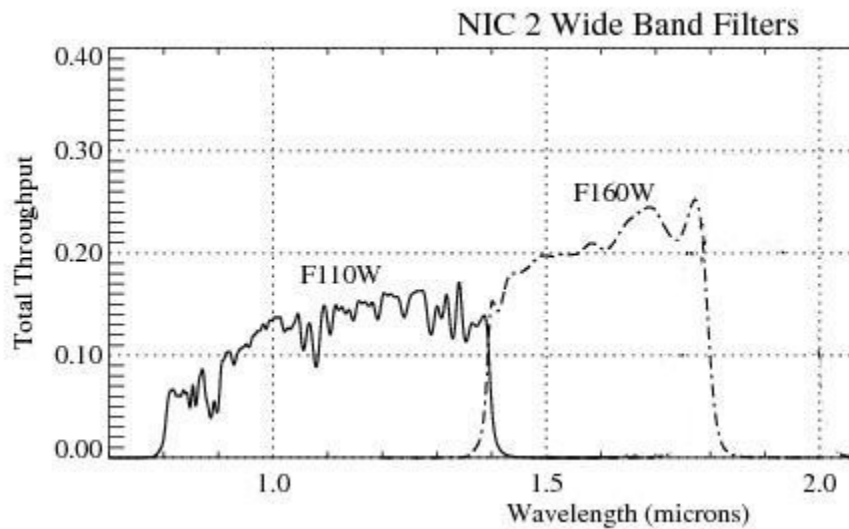


Figure 2.3 Transmission profiles of *J* (F110W) and *H* (F160W) filter bands in NIC2. Compare with Figure 2.1. Image courtesy of STScI NICMOS handbook

features discussed earlier that are observable in that wavelength range (see Figure 2.3 and compare to Figure 2.1).

NIC3 covers the spectral range of 0.8 to 2.3 μm , which was sufficient for the project, but it is out of focus and is not used for imaging.

2.2.3 Data Reduction Pipeline

No camera's detector, or charge-coupled device (CCD), operates perfectly and there are various corrections that must be taken into account before data can be accurately reduced. The HST pipeline applies all standard corrections such as zeros, darks and flats as well as non-standard ones like vignetting. But, there was a CCD non-linearity discovered that also needs to be corrected as well as an adjustment to the image quadrants. Both of these corrections are made by the user and are discussed below.

Non-Linearity correction

There is a non-linear CCD response to photons that occurs and must be corrected by the user. At first exposure the CCD's response time is slower, but it does linearize with time. Though it is a small correction it is a necessary one for our extremely dim objects and HST has provided an Image Reduction and Analysis Facility (IRAF) package that makes this correction possible. More information about non-linearity corrections can be obtained on the [STScI](#) website (Bohlin et al. 2006; de Jong et al. 2006).

Pedsky correction

Each quadrant in the NIC2 camera has a different photon response rate. When viewing raw images of any observation, each quadrant is clearly different from the others (see Figure 2.4 Left). The problem arises when the object of interest is not located in the center of one of the quadrants. If the target is close to the borders of the frames, it is impossible to get an accurate measurement of the background sky values because they differ so dramatically.

HST provides the pedsky IRAF package to the user that normalizes the four quadrants (see Figure 2.4 Right), giving the same average background value across the image. There are still some minor issues when crossing over the borders as Figure 2.4 shows. The borders have bad pixels that need to be avoided because of their effect on the final analysis. We simply flag them as bad and they are excluded from the evaluation. After running pedsky, background values can now be used from either side of the border.

2.3 Observational Technique

Each target was imaged following a $J-H-H-J$ filter sequence with a 5-pixel dither, or shift, in both the x - and y -directions between the H observations (Stephens & Noll 2006). Each J -filter

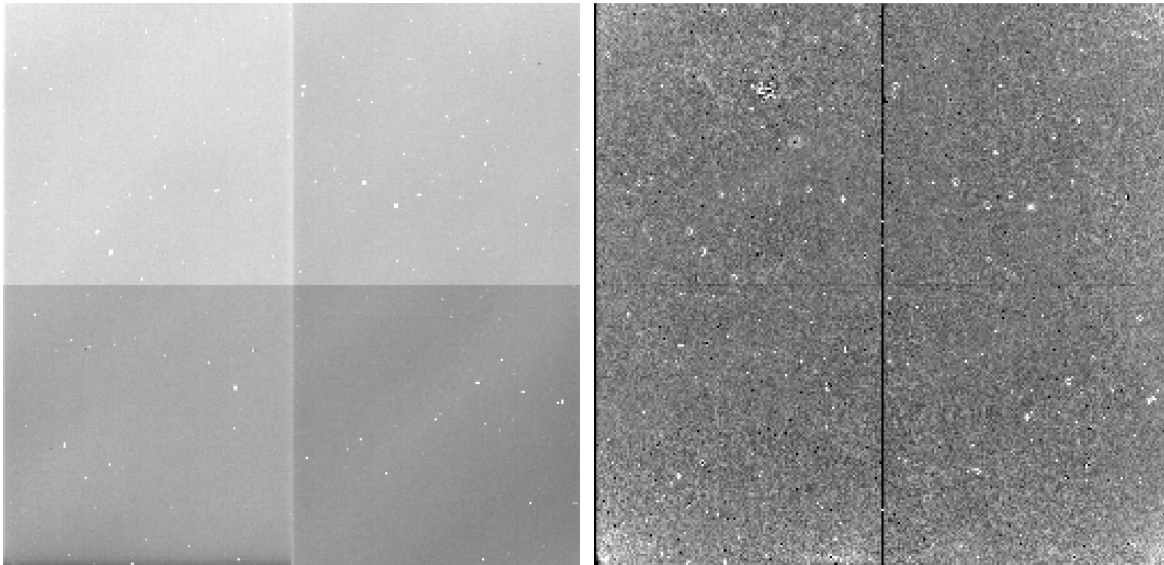


Figure 2.4 Full image from NIC2 with four independent quadrants shown. (Left) Raw, unnormalized images before pedsky applied. (Right) Normalized images after pedsky applied.

image was observed for ~ 4.2 minutes while the H -filter image integration times were about 8.4 minutes. This method allowed for ~ 25 minutes between J -filter exposures. This time frame should be sufficient to detect potential variations in the light-curve of an object, if any existed. More importantly, it was the maximum time that an object could be observed considering the time needed to change filters and other equipment and that half of HST's 90 minute orbit is 45 minutes.

With the observations, there was a high probability that, in a relatively crowded field, the target could be too close to a background star to be resolved. Each target moves more quickly across the detector than the background objects because of the relative proximity of the Kuiper belt. The J - H - H - J pattern allowed sufficient time for the KBO to move away from a nearby star as seen in Figure 2.5. With luck, we would have at least one good J -band and one good H -band image.

The dithering proved beneficial because these KBOs are very small and typically occupy anywhere from 1 to 3 pixels. One bad pixel or a cosmic ray could completely ruin the image by eliminating from 30 to 100% of the target filled pixel(s). Dithering effectively allowed HST to

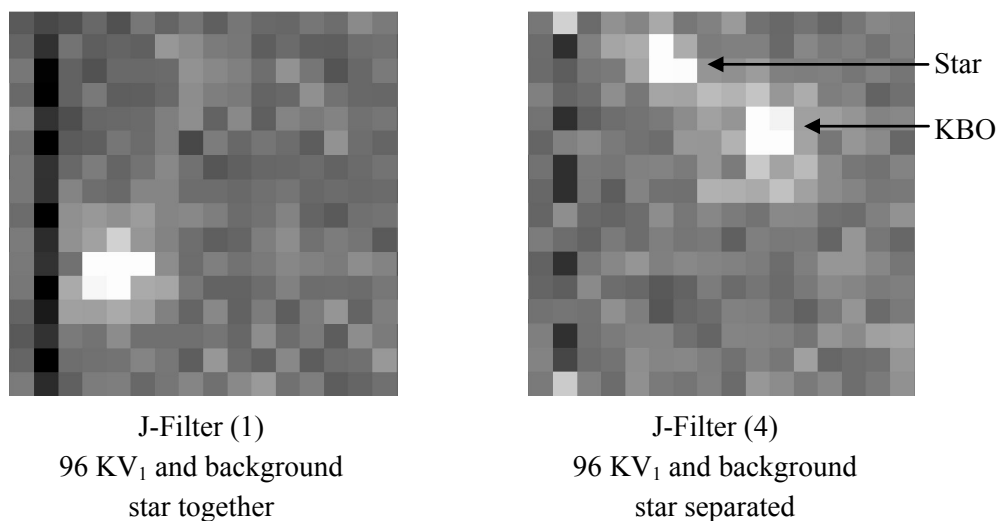


Figure 2.5 Object 96 KV₁ imaged over ~ 25 minute period illustrates how the *JHHJ* observing pattern allows a KBO to move away from a background star. The effects of dithering can be seen (see also Figure 2.6). *H*-filters omitted for clarity.

image the object from two different positions, shifting the object on the CCD by 5 pixels in both the x - and y -directions and away from any nearby bad pixels. So, now we're not only avoiding potentially bad pixels, but the KBO can more easily be identified in the image. The effectiveness of this approach can be seen in Figure 2.6 where, in this and a few other cases, two images were unusable, but the other two were still good.

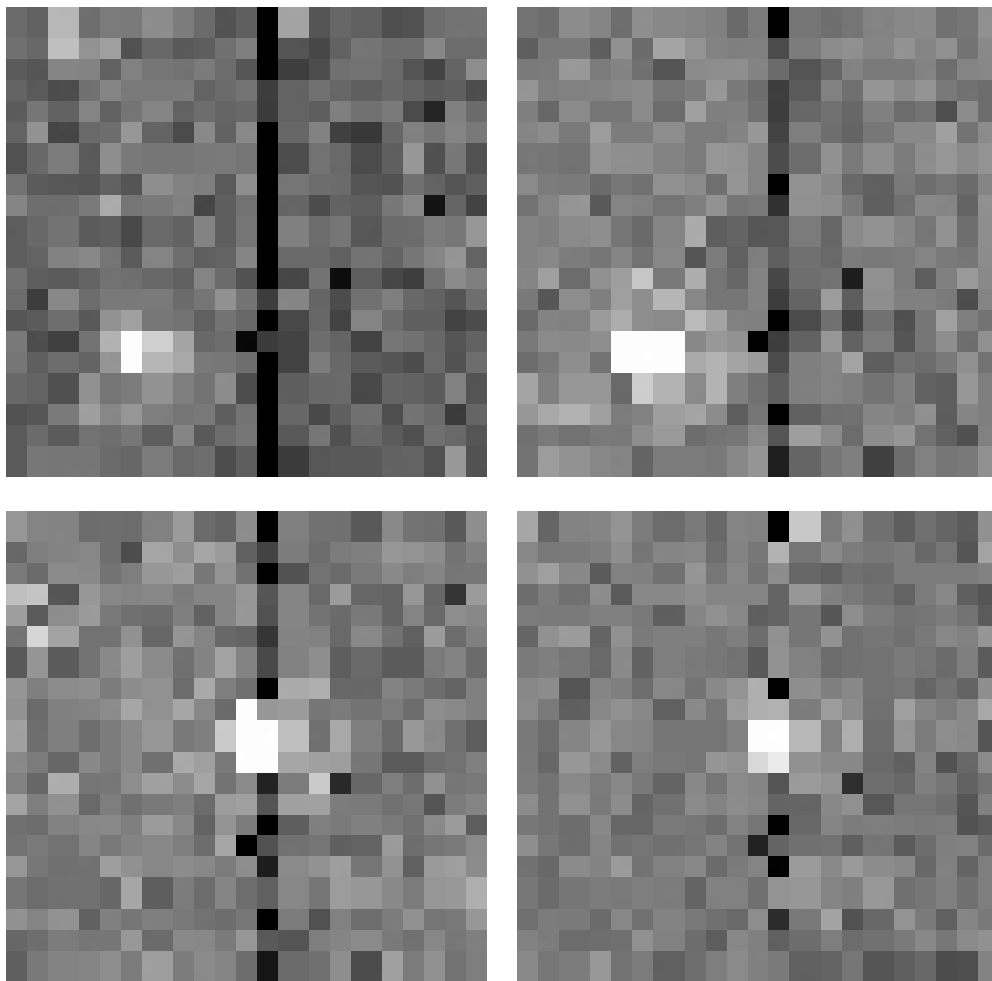


Figure 2.6 Images of object 00 CE₁₀₅ shows effectiveness of dithering. Starting at top left and following a z-pattern: *JHHJ*. The first *J* and *H* images (top two) show the KBO clear of bad pixels. The second *H* and *J* images show interference from pixels along the quadrant borders. Dithering allows us to preserve at least two images in this case.

Chapter 3

Reduction Process

The goal of our work was to obtain the near-IR photometric colors of KBOs. This chapter provides a basic definition of photometry and then describes a few approaches commonly used in acquiring photometric results. I will then describe in more detail what a point spread function (psf) is and how it relates specifically to our project. A step-by-step description of the reduction process is then laid out.

3.1 Photometry

Photometry is the process of measuring the electromagnetic intensity, or flux, of a celestial body, e.g. Kuiper belt object. Depending on the nature of the object being observed and the surrounding sky, a number of steps can be used in combination to get the best results. We used aperture and absolute photometry in conjunction with point spread function (psf) fitting for our ultimate determination of magnitudes. We first created psf models using the TinyTim (TT) program developed by John Krist and Richard Hook (2003). We fit the models to the actual data to find the best fit and to minimize error. We then applied aperture photometry on the model to determine the instrumental magnitude and converted to absolute magnitude using the recommended Vega photometric

system as a relative zero-point as detailed in Section 3.2 (See NICMOS Handbook).

3.1.1 Point Spread Modeling

A point spread function (psf) describes how a point of light is diffracted over a larger area. A celestial object that is too small to be resolved, like a KBO, will always appear as a point of light. However, diffraction due to telescopic equipment causes the light to be spread out over more pixels on the CCD with the highest concentration of light focused at the center of the psf. The faint nature of KBOs results in the occupation of only 4 - 6 pixels at the resolution of NIC2. The psf-fitting process allows us to focus on these few pixels of interest without interference from noisy background pixels.

A model of the NIC2 data can be created using TT that takes all of HST's known telescopic aberrations into consideration (see the NICMOS section of the TinyTim User's Manual by Krist and Hook 2003 for more details on these aberrations). By extracting some preliminary information from the original image through the phot package in IRAF, TT creates a model that corresponds to the position of the KBO on the detector. TT also simulates the color of the KBO by reddening the sun's spectrum to match the color of the KBO. The result is a clean model at the same position and with the same color as the KBO and no background noise.

With a model in hand, the fitting process iteratively modifies specified parameters, detailed in Section 3.2, until the discrepancy between the actual data and the model, the residuals, have been minimized. This procedure is called chi-squared (χ^2) minimization. Once minimized, the best fit, centered at the right location, is returned with a flux correction that is applied to the model, resulting in the best possible recreation of the real data. It is from this best fit that the magnitudes and colors are determined. Section 3.2 provides more details on this process (see also Stephens and Noll 2006). The model psf from which the magnitude will be extracted via aperture photometry is void of background noise and bad pixels, described next.

3.1.2 Aperture Photometry

Aperture photometry is a process of selecting an aperture, centering it on a star, and adding up all the flux. An average background value is multiplied by the number of pixels contained within the area of the aperture and then subtracted to get the flux of the object. In theory, this leaves behind only the data from the target itself. In practice, the data is left behind, but with a certain amount of error. Standard procedure for aperture photometry is to select an aperture large enough to acquire as much signal as possible while minimizing the amount of background noise.

For NIC2, the suggested aperture radius is 6.67 pixels. At πr^2 , that equates to an excessive 140 pixels. However, this size was judiciously chosen because the parameters used to convert to absolute magnitude are only calculated for an aperture of this size (see Equation 3.1). The problem with this size is that each pixel contains some uncertainty in flux arising from factors such as bias frames, background sky, cosmic rays, and/or bad pixels. Since most of the flux of our objects only occupy 4 - 6 pixels, an aperture of 6.67, encompassing so many background pixels, will only enhance the errors in our photometry. For this reason, we created a TT model, described above, and matched it to the psf of the actual object. In the fitting process, we only use the 9 brightest pixels at the center of our KBO to find the model that best recreates the data. It is *then* that we do aperture photometry on a noiseless model at 6.67 pixels. The magnitudes thus obtained are instrumental and need to be converted to an absolute scale to accurately determine magnitude and color.

Absolute photometry allows us to determine the true magnitude of our targets using a well-known, well-defined photometric system, such as Vega. In this system, Vega is used as a relative zero-point when comparing measurements of other systems. The following section contains more information concerning this conversion.

3.2 Data Reduction Process

I will now describe the process of taking the raw HST data to the point where the magnitudes of each KBO can be determined. Appendix B contains all IRAF parameter settings that were used during the process that are referenced in this section and should be set accordingly before beginning data reduction for best results. However, appropriate individual parameters will also be discussed in context.

Hubble handles all the necessary corrections mentioned in Section 2.2.2. When we received the data, we had to run the IRAF `pedsky` operation on each image so that the four camera quadrants were normalized (see Section 2.2.3) and then apply a non-linearity correction (`nlc`) (see Section 2.2.3).

There is no algorithm that will identify the object in the image field, so each J and H image was scanned by eye. This was done by blinking the images in the `ds9` image viewer. Blinking them in the *J-H-H-J* sequence allowed us to identify each object by the 5x5 pixel shift that came as a result of dithering described in Section 2.3. Since background stars moved in a different direction, finding the KBO was fairly simple, even in a field with more stars. Plus, the KBO was typically isolated and there were few to no background stars of any consequence. On a rare occasion, there was some conflict with a background object, but they were usually resolvable in at least two of the images.

Once the object is manually identified, IRAF's `imexamine` was used to determine which pixel was the central bright one. The x - / y -coordinates were then entered into an external text file to be accessed when running `phot`. `Phot` is then run using the

```
phot imagename.fits[sci] "" coord = external coordinate file
```

command line sequence with the apertures of 2, 3, and the recommended 6.67 pixel radii being set in the `photpars` task package. Set the `phot.fitskypars.salgori` parameter to *ofilter* for the original

image so the background (msky) value can be interpreted properly. Otherwise, it will do photometry with a constant background or some other, more complicated, algorithm and the values will be wrong. Then set the annulus inner radius to 20 with a width of 20 pixels in the same parameter package. This annulus setting allows us to collect a large area of background pixels that are a fair distance from the object, thus avoiding any light from the object itself. There was little concern about interference with neighboring objects because most KBOs were isolated. The purpose of such a large annulus is to obtain the best background average possible while reducing the effects of any bad pixels. If there are stars nearby or if the KBO is too close to the image sutures, then a manual approach should be used to determine the background value.

Phot produces an `imasename.mag.1` file that contains all of the information about the image. The IRAF `txdump` command

```
txdump imasename.mag.1 xshift,yshift,msky,stdev,flux yes > external file name
```

is used to extract the x - / y -shift, msky, stdev, and flux (flux per pixel, or dn for later flux correction) fields from the phot output file. The `>` pipes the data to an external file. These preliminary results are used to determine a color correction value (ebmv) that is used by TinyTim (Krist and Hook (2003)) to create models from which the final analysis is made. Since the light we observe from the KBOs is reflected sunlight, TT uses the ebmV value to redden the sun's spectrum to match the color of the KBO's surface. A detailed, step-by-step layout for producing these models using TT, along with the appropriate user input, is provided in Appendix A.

The model that is created by TT is a .fits image that is sub-sampled by a factor of 10. However, the next steps in the process require a text file rather than images. So, the image is converted into a text file using the IRAF `wtext` command,

```
wtext @infile.nic2.list model .
```

Wtext outputs each pixel value of the model to an external list according to the input file `infile.nic2.list`. This file instructs wtext to create 100 different models from the original by, first,

eliminating a solitary column and no rows. Next, that same column is eliminated accompanied by a row. This is repeated with the original column until 10 rows have been removed. After that loop is complete, two columns are deleted followed by the same row elimination pattern as the first column. This will repeat until 10 columns have been deleted with 10 rows in tow. The amazing result is that the center of each model is shifted ever so slightly by 0.1 pixels in x and/or y.

A Fortran program called `binnic.f`, written by Dr. Stephens, is then used to bin each model that is $\leq 179 \times 179$ pixels down to a 17×17 array. The \leq arises from the removal of the columns and rows described above. Clearly, $17 \times 17 \neq 179$, so the excess pixels beyond the edge of a model larger than 170×170 are discarded as they make no contribution to the model anyway. The binning is accomplished by taking 10 pixels in x and y and combining them into one. Binnic outputs 100 `prim.psf` model text files, each one of which has a different sub-pixel center and is now capable of acquiring sub-pixel variations in the psf. With this compression complete, we can run the fitting program - `nicpsf`.

One of the great advantages of using this method is that when TT creates the models, it does not assume the data from HST is gaussian, or any other predefined function for that matter, as does IRAFs `psfmeasure` for example. TT uses the actual, well-known, HST specific telescopic affects as described in the previous section. But, saying this is **one** of the advantages implies that there might be others, which, in fact, there is. Another advantage of using this method is that the models are clear of any background noise. Even though the actual data is not, we obtain the best background average that we can and then subtract that from the target before running the fitting process. This way we can now focus our efforts on only those few pixels that contain all the information.

We start by using

```
listpix imagename[cx-1:cx+1,cy-1:cy+1] > objectname.txt
```

to get the values of the pixels immediately around the object from the *original* HST image, where `cx` and `cy` are the centers in x and y, respectively, \pm the given value - in this case ± 1 . The center

pixel has the coordinates that you determined by visual inspection at the beginning. The `listpix` command will extract the pixel values in a 3×3 array and stores them in an external file (`3x3.txt` for simplicity). These nine pixels are what the `nicpsf` will be attempting to fit. The user then creates a file called `inpar.txt` that contains "`3x3.txt`" along with `msky` and `stdev` values obtained from the original phot, one per line (see Figure 3.1).



Figure 3.1 Input file for `nicpsf`. First line - the file that contains the 3×3 array from the original image. Second line - background value (`msky`) obtained from the original phot operation. Third line - `stdev` obtained from the original phot operation.

Running `nicpsf` reads `inpar.txt` and takes the models with the shifted centers and iteratively compares them to the HST image by first modifying the `x` and `y` parameters while holding the flux constant. Once the best fit is found by this method, then `x` and `y` are held constant while the flux is adjusted until the fit is minimized. This process is repeated over and over until the fit with the lowest statistical error is found and the model is the best possible recreation of the data. `Nicpsf` returns `single.out` with the best model fit and a flux adjustment value which is later added to the model via the IRAF `imarith` command. I should mention here that even though we selected the fit with the lowest residuals, there are actually multiple model fits that can legitimately be used as a good fit, each with its own flux scaling factor. `Nicpsf` records each attempted fit in the `chi.out.csv` and `fit.out.csv` files and these are used later to determine the errors in the magnitudes and colors (see Chapter 4).

You are now ready to run

```
rtext prim.model.psf prim.model.fits ,
```

which converts the best model, `prim.model.psf`, into a `.fits` image, `prim.model.fits`. Once the model

has been converted into an image, running

```
imarith prim.model.fits * flux finalimagenname.fits
```

will take the model image and apply the flux correction found by the nicpsf fitting program so that the flux of the model matches that of the real object. This file is now the fully corrected image from which you will determine the magnitudes and colors. You are working with a model with no background. Previously you ran a phot fitsky algorithm that calculated the best background average. With no background, change the phot parameters phot.fitsky.salgori and .skyvalue to "constant" and "0", respectively, and rerun phot and txdump just as you did before. The values extracted here are now used to calculate the true flux of the object with the formula

$$F_i = \frac{dn_i \times phot\ fnu_i \times apcorr_i}{zpvega} = \frac{F(kbo)}{F(Vega)} \quad \dots i = J, H, \quad (3.1)$$

where

dn_i = flux value from txdump command, at the recommended aperture of 6.67 pixels,

$phot\ fnu_i$ = bandpass-averaged flux densities, used to convert counts to flux units,

$apcorr_i$ = aperture correction,

$zpvega$ = flux to magnitude conversion from a zero magnitude star.

The photfnu, apcorr, and zpvega are filter specific keywords for NICMOS 2 correction values available on the [STScI](#) website. The magnitude for each filter is then determined by

$$M_i = -2.5 \times \log(F_i) \quad \dots i = J, H. \quad (3.2)$$

and the color is calculated using

$$(M_J - M_H) = J_{avg.} - H_{avg.} \quad (3.3)$$

The results of this reduction process can be found in Chapter 4. A condensed layout of the entire process can be found in Figure 3.2 below. Before running the process parameters should be set according to Appendix B.

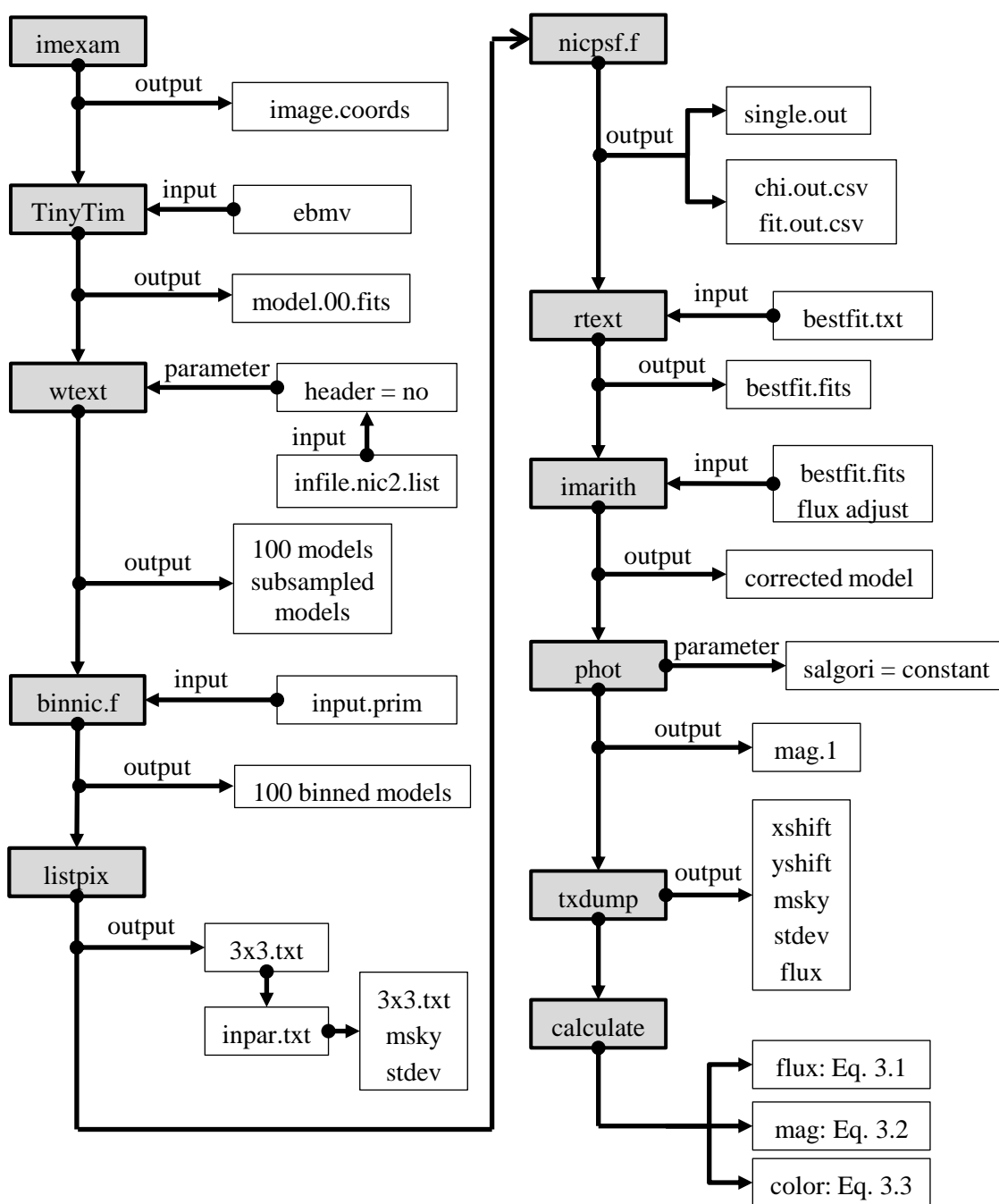


Figure 3.2 Outline intended as a guide through the reduction process. Grey boxes are the main operations. White boxes are parameter changes, function input and output.

Chapter 4

Results and Conclusions

Photometry for all 80 KBOs observed with NIC2 is laid out in Table 4.1. Almost all of these were not previously observed. They range in magnitude from $23.3 \leq m_{F110W} \leq 19.1$ and $22.5 \leq m_{F160W} \leq 18.6$ (00 PH₃₀ and 26375, respectively). Colors range in value from -0.274 (99 OY₃) to 0.831 (97 CS₂₉).

In studying the larger KBOs, previous work has found that they are blue and highly reflective, suggestive of the presence of surface ice. When objects such as Pluto and Eris reach perihelion, increased solar radiation results in sublimation of surface materials. These larger objects are just big enough to retain a thin atmosphere. However, as they approach aphelion, the temperatures are much colder and the atmosphere freezes out. When this happens, there is some precipitation that accumulates as fresh ice on the surface, resulting in their very blue appearance. In the case of Eris, the result is a very reflective surface with an albedo of ~ 1 (Sicardy et al. 2011a;b).

From these studies, it was anticipated that the Kuiper belt as a general body would display similar features. From the results tabulated in Table 4.1, we found that only 3% of our targets were blue relative to the sun (colors < 0.42), but they are not big enough to retain an atmosphere (see Section 1.3.1). However, these were readily identified with the EL 61 (Haumea) collisional family, whose blue nature is a result of a collision which stripped off its hydrocarbon surface (Ragozzine

& Brown 2007).

The rest of our targets were red relative to the sun (colors > 0.42). This was a somewhat unexpected result and we are unable to come to any conclusion about the ice composition of the Kuiper belt. This implies that there has been a great deal of weathering that has covered the ices as described in Section 1.3.2. However, we did detect some slight, albeit statistically insignificant, variation in the colors of the classical belt objects.

Figure 4.1 shows 34 objects belonging to the classical Kuiper belt (cubewanos). We excluded two of the bluest objects, 24835 (1995 SM₅₅) and 99 OY₃, known to belong to the Haumea collisional family. It should be noted that though the blue dots represent the bluest of this set, they are still red relative to the sun's spectrum and are merely less red than the others. The x-axis corresponds to the semi-major axis. We found that the bluest objects trend closer to the sun, whilst those that are the reddest, seem to trend farther away from the sun in an apparent color gradient. The implication of such a finding is that KBOs formed at different locations with different abundances of ice relative to one another. We emphasize that this trend appears in the IR and not in the visible. It is also important to note that this trend only appears to occur in the extreme colors and not in the middle.

With this small of a collection it is difficult to confirm, with any statistical significance, the existence of a color gradient. A larger data set needs to be obtained that will allow us to either confirm or refute this finding.

Table 4.1. Orbital Parameters and Photometry

Object Name	Class	Distance (AU)	Ellipticity (e)	Inclination (i)	Mag (<i>J</i>) F110W	Mag (<i>H</i>) F160W	Color (<i>J</i> - <i>H</i>)
00AF255	unclassified	49.081	0.256	30.879	21.436	20.778	0.659
00CE105	cubewano	44.200	0.063	0.549	21.758	21.490	0.269
00CF105	cubewano	44.193	0.044	0.529	23.001	22.433	0.569
00CG105	cubewano	46.642	0.039	27.906	22.261	21.543	0.719
00CK105	plutino	39.633	0.226	8.104	21.980	21.442	0.538
00CL104	cubewano	44.754	0.083	1.240	21.714	21.075	0.639
00CM105	cubewano	42.488	0.070	3.756	21.625	21.115	0.453
00CO105	cubewano	47.339	0.143	19.205	21.673	21.136	0.537
00CP104	cubewano	44.548	0.096	9.465	22.259	21.633	0.626
00CQ105	Res(2:5)	57.439	0.393	19.625	22.155	21.550	0.605
00CQ114	cubewano	46.441	0.118	2.694	22.429	21.962	0.462
00CR105	unclassified	229.638	0.807	22.700	22.640	22.057	0.610
00FE8	Res(2:5)	55.813	0.408	5.858	21.182	20.514	0.669
00OJ67	cubewano	42.601	0.018	1.114	21.209	20.668	0.527
00OK67	cubewano	46.293	0.136	4.896	21.076	20.462	0.614
00OU69	cubewano	42.961	0.044	4.421	21.438	20.886	0.552
00PD30	cubewano	46.284	0.019	4.618	21.861	21.127	0.733
00PE30	SDO	54.022	0.339	18.454	20.815	20.167	0.647
00PH30	SDO	76.397	0.500	8.076	23.303	22.507	0.796
00PJ30					22.933	22.339	0.594
00PV29					22.924	22.256	0.668
00YW134	unclassified	58.439	0.295	19.761	19.716	19.157	0.560
01KD77	plutino	39.475	0.114	2.253	20.253	19.659	0.593
01KP77	unclassified	43.480	0.187	7.204	21.384	20.856	0.529
01KY76	plutino	39.274	0.236	3.971	21.187	20.663	0.524
01OG109	cubewano	43.292	0.011	0.552	22.930	22.430	0.500
01OK108	cubewano	42.721	0.033	1.998	22.517	21.936	0.582
01QC298	cubewano	46.111	0.120	30.646	21.768	21.203	0.594
01QX322	SDO	59.990	0.422	28.509	21.311	20.718	0.594
01XS254	unclassified	37.500	0.060	4.253	21.801	21.205	0.596

Table 4.1 (continued)

Object Name	Class	Distance (AU)	Ellipticity (e)	Inclination (i)	Mag (<i>J</i>) F110W	Mag (<i>H</i>) F160W	Color (<i>J</i> - <i>H</i>)
01XU254	cubewano	43.863	0.095	6.498	21.313	20.799	0.515
93FW	cubewano	43.874	0.050	7.742	21.633	21.083	0.550
95TL8					19.511	18.880	0.234
96KV1	cubewano	45.052	0.108	8.098	21.223	20.611	0.611
96RQ20	cubewano	43.829	0.010	31.712	21.469	20.943	0.526
97CQ29	cubewano	45.510	0.124	2.896	22.747	22.351	0.396
97CS29	cubewano	44.188	0.017	2.233	20.466	19.884	0.831
97CT29	cubewano	44.049	0.025	1.017	21.888	21.309	0.583
97CV29	cubewano	42.507	0.053	8.009	21.879	21.384	0.496
97RT5	unclassified	41.160	0.028	12.758	21.897	21.384	0.513
98FS144	cubewano	42.011	0.022	9.868	21.790	21.247	0.543
98KG62	cubewano	43.192	0.055	0.797	21.850	21.281	0.569
98KY61	cubewano	44.119	0.051	2.055	22.554	22.055	0.499
98UU43	Res(3:4)	36.516	0.127	9.569	21.578	20.891	0.687
98WA25	cubewano	42.694	0.029	1.047			
98WX31	cubewano	45.694	0.112	2.976	21.211	20.657	0.554
98WY24	cubewano	43.438	0.046	1.911	21.611	21.049	0.562
98WZ31	plutino	39.677	0.170	14.603	22.051	21.476	0.575
99CD158	cubewano	43.932	0.140	25.403	20.664	20.065	0.600
99CF119	SDO	90.588	0.273	1.475	21.601	21.074	0.527
99CH119	cubewano	43.587	0.573	19.664	22.845	22.428	0.417
99CJ119	cubewano	45.704	0.077	19.902	21.707	21.056	0.651
99CL119	cubewano	47.222	0.074	3.191	21.962	21.041	0.651
99CQ133	unclassified	41.563	0.013	23.226	22.244	21.576	0.669
99CX131	unclassified	42.537	0.232	9.732	22.140	21.617	0.523
99HC12	unclassified	45.486	0.241	15.350	22.274	21.582	0.692
99HJ12	cubewano	43.065	0.043	4.545	21.942	21.698	0.245
99OD4	unclassified	41.239	0.098	14.446	22.115	21.455	0.660
99OE4	cubewano	45.123	0.042	2.154	21.517	21.015	0.502
99OF4	cubewano	44.726	0.066	2.664	21.660	21.128	0.533

Table 4.1 (continued)

Object Name	Class	Distance (AU)	Ellipticity (e)	Inclination (i)	Mag (<i>J</i>) F110W	Mag (<i>H</i>) F160W	Color (<i>J</i> - <i>H</i>)
99OH4	unclassified	40.293	0.037	28.256	null	22.110	0.539
99OJ4	unclassified	37.886	0.027	4.005	21.602	21.121	0.484
99OY3	unclassified	43.616	0.167	24.295	21.766	22.039	-0.274
99RC215	cubewano	43.976	0.056	1.403	22.015	21.548	0.466
99RY215	unclassified	45.045	0.234	22.234	21.690	21.008	0.681
99RZ253	cubewano	43.584	0.087	0.562	21.231	20.889	0.342
15788	plutino	39.369	0.322	1.944	21.468	20.833	0.636
15789	plutino	39.449	0.183	5.170	20.641	20.016	0.625
15809	Res(3:5)	42.085	0.214	14.052	21.927	21.287	0.640
15810	plutino	39.262	0.115	3.806	21.488	20.880	0.609
15874	SDO	83.934	0.583	23.979	19.689	19.253	0.436
15883	unclassified	47.381	0.215	19.107	22.301	21.600	0.701
19255	cubewano	42.990	0.034	1.489	22.236	21.520	0.716
19521	cubewano	45.935	0.108	12.034	19.613	19.064	0.548
20161	Res(1:2)	47.698	0.397	12.452	21.764	21.091	0.673
24835	cubewano	41.866	0.107	27.071	19.658	19.818	-0.160
26375	Res(2:5)	56.122	0.425	7.600	19.136	18.635	0.501
33001	cubewano	43.756	0.033	1.450	21.516	20.949	0.567
33340	plutino	39.479	0.256	3.036	19.847	19.310	0.537
42301	SDO	51.447	0.281	0.754	19.454	18.833	0.621
45802	cubewano	43.219	0.012	1.178	22.924	22.354	0.570

Note. — Cubewano = classical - hot or cold depending on orbital inclination; SDO = scattered disc object $\Rightarrow e \leq 0.80$, $i \leq 40^\circ$, $a > 30$ AU; plutino = objects in a 2:3 resonance with Pluto (see Section 1.3.5). See (Benecchi et al. 2011) for additional information.

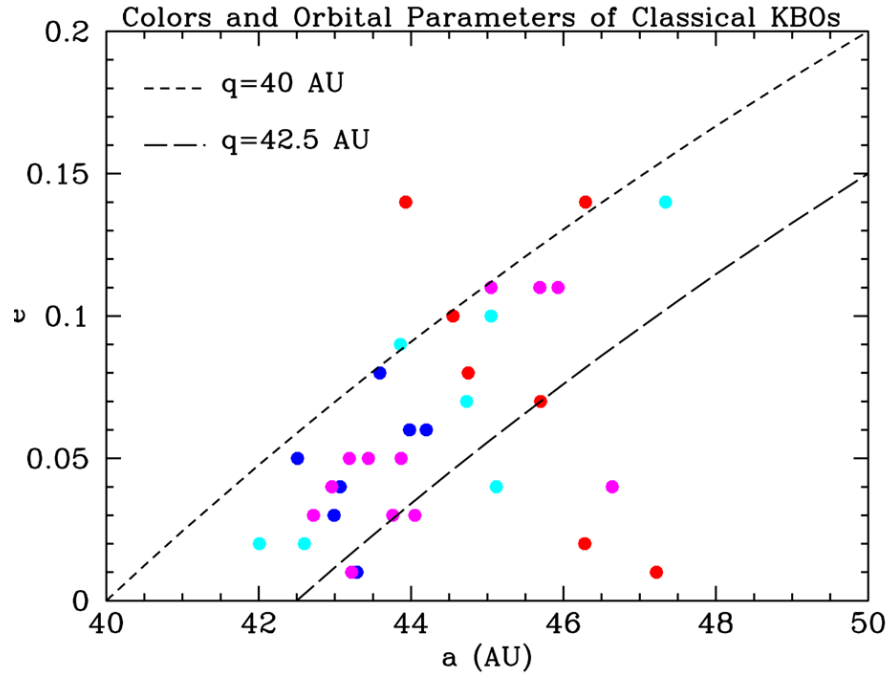


Figure 4.1 A plot of the semi-major axis vs. eccentricity for all of the classical KBOs in our data set. We excluded objects 24835 (1995 SM₅₅) and 99 OY₃, which are known members of the EL 61 collision family (Haumea). These 34 classical KBOs had $J-H$ colors ranging from 0.38 to 0.84. Natural breaks seem to occur between groups of objects at $J-H$ values of 0.50, 0.55, and 0.60. Natural breaks were used to color code the plot to identify if any possible color correlations. The colors in the plot correspond to: Dark Blue $\rightarrow J-H < 0.50$, Cyan $\rightarrow 0.50 < J-H < 0.55$, Magenta $\rightarrow 0.55 < J-H < 0.60$, Dark Red $\rightarrow 0.60 < J-H$.

Appendix A

TinyTim

TinyTim (TT) (Krist and Hook 2003) is executed in a standard terminal rather than xgterminal (TT download and user manual available at <http://www.stsci.edu/hst/observatory/focus/TinyTim>). The full input/output is provided below. User input is marked by bold and larger text. If TT is not running on the computer, use the simple instructions for a Bash shell provided in the TinyTim user manual to install it. The input required by the user is described below with screen shots of the interface on the following pages. User input is in bold type-face.

The first user input calls `tiny1` and requires the `ebmv` coefficient value discussed in Section 3.2. The next input is `20` which identifies the camera used for observation and, in the case of NIC2, if it was before or after the service mission to add the cryogenic cooling system. The position input is the coordinates that you obtained from scanning the images by eye. Our targets were all observed after September 29, 2002 and the next input is `'y'`. The parameters are different if a target was observed prior to that date. The filters we used were *J* (F110W) and *H* (F160W). The spectrum option is `'5'` and the name of the input file we used is `sunkurucz.tab`. This file contains values of the sun's spectrum that TT uses when creating a corrected model. We used the recommended diameter of 3 arcseconds for the model psf and subsampled it with an oversampling factor of 10. This creates a model with a 179×179 array of pixels which we named `'model'` for convenience.

TT then prompts you with the input for tiny2 which creates the model based on the data you have provided. The model produced is a .fits image as described in Section 3.1.1 and Section 3.2 discusses what is to be done with the image.

rawli2@C430ESC-02:/pathname\$ **tiny1 ebmv=.380**

----- Tiny Tim v6.3 : The HST PSF Generator -----

Release Date : June 15, 2004

Developed by John Krist

Additional support by Richard Hook

>> Manual in /software/tinytim/6.3/tinytim.pdf <<

** <http://www.stsci.edu/software/tinytim> **

----- Aberrated Cameras ----- ----- Corrected HST Optics -----

- | | |
|------------------------------|------------------------------|
| 1) Wide Field Camera (WFPC1) | 5) WFPC2 - Wide Field Camera |
| 2) Planetary Camera (WFPC1) | 6) WFPC2 - Planetary Camera |
| 3) FOC f/48 | 7) COSTAR-corrected FOC f/48 |
| 4) FOC f/96 | 8) COSTAR-corrected FOC f/96 |

---- Second Generation ----

----- Third Generation -----

- | | |
|--------------------------------------|--|
| 9) NICMOS Camera 1 (pre-cryocooler) | 15) ACS - Wide Field Channel |
| 10) NICMOS Camera 2 (pre-cryocooler) | 16) ACS - High Resolution Channel |
| 11) NICMOS Camera 3 (pre-cryocooler) | 17) ACS - HRC coronagraph off-spot PSF |
| 12) STIS CCD | 18) ACS - Solar Blind Channel |
| 13) STIS NUV-MAMA | 19) NICMOS Camera 1 + cryocooler |
| 14) STIS FUV-MAMA | 20) NICMOS Camera 2 + cryocooler |
| | 21) NICMOS Camera 3 + cryocooler |

Choice : **20**

Enter position (x and y) on detector in INTEGER
pixels (range = 0-255) or the filename of a list
of positions preceded by a '@' (ie. @xy.lis).

Position : **194 162**

Is the observation after September 29, 2002? (Y/N) : **y**

Select filter passband :

- Enter the name of the filter (eg. f555w)
- Enter MONO to specify a single wavelength

Filter : **f110w**

31 wavelengths will be used to generate PSF

Choose form of object spectrum :

- 1) Select a spectrum from list
- 2) Blackbody
- 3) Power law : $F(\nu) = \nu^i$
- 4) Power law : $F(\lambda) = \lambda^i$
- 5) Read user-provided spectrum from ASCII table

Choice : **5**

NOTE : Spectrum MUST have < 15000 points and be
in Angstrom and flux pairs (see manual for flux types).

Enter name of spectrum file : **sun**

Applying extinction ...

Assuming detector pixel size of 0.07568 arcsec

The maximum computable PSF size is 30.0 arcsec.

The recommended size is about 3.0 arcseconds.

What diameter should your PSF be (in arcseconds)? : **3**

Do you wish to generate a subsampled PSF? (Y/N) : **y**

OverSampling factor along an axis (min=2, max=10) : **10**

Rootname of PSF image files (no extension) : **model**

To execute the next stage, enter the command :

tiny2 psf.list

rawli2@C430ESC-02:/pathname\$ **tiny2 psf.list**

Appendix B

IRAF Parameters

Below are the parameter settings for phot. Figure B.1 shows the iraf parameters that are required when extracting the initial values as described in Section 3.2. These settings should be used when working with the HST data. The datapars parameters ccdread and gain require keywords available in the image headers. If these values are known, then these two keywords can be left blank and the values entered into readnoise and epadu.

Figure B.2 shows the same set of parameters with the appropriate and necessary changes when working with the model. It will be noted in Figure B.1 that the salgorithm parameter under fit-skypars is shown set to "ofilter" for the data. This is required for the HST data as described in Section 3.2. When the model has been created, this setting must be changed to "constant" as shown in Figure B.2, which accounts for the fact that the background is void of noise. The double quotes, "", are shown merely for consistency and clarity. They are not needed for an entry.

Phot			centerpars		
image	=	"image.fits"	calgorithm	=	"centroid"
skyfile	=	""	cbox	=	5
coords	=	""	cthreshold	=	0
output	=	"default"	minsratio	=	1
plotfile	=	""	cmaxiter	=	10
datapars	=	""	maxshift	=	1
centerpars	=	""	clean	=	no
fitskypars	=	""	rclean	=	1
photpars	=	""	rclip	=	2
interactive	=	no	kclean	=	3
radplots	=	no	mkcenter	=	no
icommands	=	""			
gcommands	=	""	fitskypars		
wcsin	=	_.wcsin	salgorithm	=	"ofilter"
wcsout	=	_.wcsout	annulus	=	20
cache	=	_.cache	dannulus	=	20
verify	=	no	skyvalue	=	0
update	=	no	smaxiter	=	10
verbose	=	no	sloclip	=	0
graphics	=	_.graphics	shiclip	=	0
display	=	_.display	snreject	=	50
			sloreject	=	3
datapars			shireject	=	3
scale	=	1	khist	=	3
fwhmpsf	=	2.5	binsize	=	0.1
emission	=	yes	smooth	=	no
sigma	=	INDEF	rgrow	=	0
datamin	=	INDEF	mksky	=	no
datamax	=	INDEF			
noise	=	"poisson"	photpars		
ccdread	=	""	weighting	=	"constant"
gain	=	""	apertures	=	"2,3,6.67"
readnoise	=	""	zmag	=	25
epadu	=	""	mkapert	=	no
exposure	=	""			
airmass	=	""			
filter	=	""			
obstime	=	""			
itime	=	1			
xairmass	=	INDEF			
ifilter	=	"INDEF"			
otime	=	"INDEF"			

Figure B.1 IRAF parameters required when photing original data.

Phot			centerpars		
image	=	"image.fits"	calgorithm	=	"centroid"
skyfile	=	""	cbox	=	5
coords	=	""	cthreshold	=	0
output	=	"default"	minsratio	=	1
plotfile	=	""	cmaxiter	=	10
datapars	=	""	maxshift	=	1
centerpars	=	""	clean	=	no
fitskypars	=	""	rclean	=	1
photpars	=	""	rclip	=	2
interactive	=	no	kclean	=	3
radplots	=	no	mkcenter	=	no
icommands	=	""			
gcommands	=	""	fitskypars		
wcsin	=	_.wcsin	salgorithm	=	"constant"
wcsout	=	_.wcsout	annulus	=	20
cache	=	_.cache	dannulus	=	20
verify	=	no	skyvalue	=	0
update	=	_.update	smaxiter	=	10
verbose	=	_.verbose	sloclip	=	0
graphics	=	_.graphics	shiclip	=	0
display	=	_.display	snreject	=	50
			sloreject	=	3
datapars			shireject	=	3
scale	=	1	khist	=	3
fwhmpsf	=	2.5	binsize	=	0.1
emission	=	yes	smooth	=	no
sigma	=	INDEF	rgrow	=	0
datamin	=	INDEF	mksky	=	no
datamax	=	INDEF			
noise	=	"constant"	photpars		
ccdread	=	""	weighting	=	"constant"
gain	=	""	apertures	=	"2,3,6.67"
readnoise	=	0	zmag	=	25
epadu	=	1	mkapert	=	no
exposure	=	""			
airmass	=	""			
filter	=	""			
obstime	=	""			
itime	=	1			
xairmass	=	INDEF			
ifilter	=	"INDEF"			
otime	=	"INDEF"			

Figure B.2 IRAF parameters required when photing the model. Necessary changes have been set in bold for clarification.

Bibliography

- Benecci, S. D., Noll, K. S., Stephens, D. C., Grundy, W. M., & Rawlins, J. 2011, *Icarus*, 213, 693
- Bohlin, R. C., Riess, A., & de Jong, R. 2006, NICMOS Count Rate Dependent Non-Linearity in G096 and G141, Tech. rep.
- de Bergh, C., Delsanti, A., Tozzi, G. P., Dotto, E., Doressoundiram, A., & Barucci, M. A. 2005, *A&A*, 437, 1115
- de Jong, R. S., Bergeron, E., Riess, A., & Bohlin, R. 2006, NICMOS count-rate dependent nonlinearity tests using flatfield lamps, Tech. rep.
- Doressoundiram, A., Boehnhardt, H., Tegler, S. C., & Trujillo, C. 2008, "Color Properties and Trends of the Transneptunian Objects", ed. Barucci, M. A., Boehnhardt, H., Cruikshank, D. P., Morbidelli, A., & Dotson, R., 91–104
- Gladman, B., Marsden, B. G., & Vanlaerhoven, C. 2008, "Nomenclature in the Outer Solar System", ed. Barucci, M. A., Boehnhardt, H., Cruikshank, D. P., Morbidelli, A., & Dotson, R., 43–57
- Hudson, R. L., Palumbo, M. E., Strazzulla, G., Moore, M. H., Cooper, J. F., & Sturmer, S. J. 2008, Laboratory Studies of the Chemistry of Transneptunian Object Surface Materials, ed. M. A. Barucci, H. Boehnhardt, D. P. Cruikshank, A. Morbidelli, & R. Dotson, 507–523

- Jewitt, D., Luu, J., & Marsden, B. G. 1992, IAU Circ., 5611, 1
- Jewitt, D. C., & Luu, J. 2004, Nature, 432, 731
- Jewitt, D. C., & Luu, J. X. 2001, AJ, 122, 2099
- Licandro, J., Pinilla-Alonso, N., Pedani, M., Oliva, E., Tozzi, G. P., & Grundy, W. M. 2006, A&A, 445, L35
- Morbidelli, A. 2005, ArXiv Astrophysics e-prints
- Morbidelli, A., & Levison, H. F. 2003, nature, 422, 30
- Ragozzine, D., & Brown, M. E. 2007, AJ, 134, 2160
- Schlichting, H. E., Ofek, E. O., Wenz, M., Sari, R., Gal-Yam, A., Livio, M., Nelan, E., & Zucker, S. 2009, Nature, 462, 895
- Sicardy, B., et al. 2011a, Nature, 478, 493
- Sicardy, B., et al. 2011b, in EPSC-DPS Joint Meeting 2011, 137
- Stephens, D. C., & Noll, K. S. 2006, AJ, 131, 1142
- Tegler, S. C., Grundy, W. M., Romanishin, W., Consolmagno, G. J., Mogren, K., & Vilas, F. 2007, AJ, 133, 526
- Viana, A., et al. 2009, NICMOS Instrument Handbook, 11th edn., Space Telescope Science Institute (STScI), Baltimore, Maryland

Index

- binnic, 27
- Classical Belt, 2
 - Cold, 4
 - Hot, 5
- Color
 - definition, 9
 - Equation 3.3, 29
- dither, 18
- ebmv value, 26
- Edgeworth, Kenneth, 1
- Flux
 - Equation 3.1, 29
- Hubble Space Telescope (HST)
 - Equipment (NICMOS), 14
 - Filters, 16
- IRAF, 18
 - imarith, 28
 - imexamine, 25
 - listpix, 27
 - parameters, 41
 - phot, 25
 - rtext, 28
 - txdump, 26
 - wtext, 26
- KBO Characteristics
 - Blue, 9
 - Hydrocarbons, Tholins, 8
 - Ice, 5, 7, 13
 - Red, 9
 - Thermal Radiation, 8
- Kuiper, Gerard, 1
- Magnitude
 - Equation 3.2, 29
- nicpsf, 28
- Non-linearity correction, 18
- pedsky correction, 18
- Photometry
 - Absolute, 24
 - Aperture, 24
 - definition, 22
 - Point Spread Function (psf), 23
- TinyTim, 23
 - instructions, 37